

Unlocking the Keyhole: H₂ and PAH emission from molecular clumps in the Keyhole Nebula

K. J. Brooks,^{★†} M. G. Burton, J. M. Rathborne, M. C. B. Ashley and J. W. V. Storey

School of Physics, The University of New South Wales, Sydney, NSW 2052, Australia

Accepted 2000 June 19. Received 2000 June 2; in original form 2000 January 25

ABSTRACT

To better understand the environment surrounding CO emission clumps in the Keyhole Nebula, we have made images of the region in H₂ 1–0 S(1) (2.122- μ m) emission and polycyclic aromatic hydrocarbon (PAH) emission at 3.29 μ m. Our results show that the H₂ and PAH emission regions are morphologically similar, existing as several clumps, all of which correspond to CO emission clumps and dark optical features. The emission confirms the existence of photodissociation regions (PDRs) on the surface of the clumps. By comparing the velocity range of the CO emission with the optical appearance of the H₂ and PAH emission, we present a model of the Keyhole Nebula whereby the most negative velocity clumps are in front of the ionization region, the clumps at intermediate velocities are in it and those which have the least negative velocities are at the far side. It may be that these clumps, which appear to have been swept up from molecular gas by the stellar winds from η Car, are now being overrun by the ionization region and forming PDRs on their surfaces. These clumps comprise the last remnants of the ambient molecular cloud around η Car.

Key words: ISM: clouds – ISM: globules – ISM: individual: Carina Nebula – ISM: kinematics and dynamics – ISM: molecules.

1 INTRODUCTION

The Keyhole Nebula is part of the Carina Nebula, a star-forming/giant molecular cloud (GMC) complex, containing some of the most massive stars known in our Galaxy. It is bathed in the UV radiation field from the nearby open star cluster, Tr 16. This cluster contains numerous O-type stars, including three O3 stars (Walborn 1995). It is at a distance of 2.2 kpc (Tovmassian 1995) and is centred on one of the most massive stars known – η Car, which has a present-day mass of about 120 M_⊙ (Davidson & Humphreys 1997). The optical image of the Keyhole Nebula taken by Malin (1993) reveals many interesting features such as dark patches and filaments, the most prominent being in the shape of an old-fashioned keyhole, which gave the nebula its name (see Fig. 1a). Herschel (1847) was the first to note this peculiar feature and likened it to the shape of a ‘lemniscata’. Some of the smaller features also have bright rims. This is beautifully illustrated in the recent colour-composite image taken with NASA’s Hubble Space Telescope.¹

The molecular gas in this region is highly inhomogeneous,

breaking into several clumps which are all associated with the dark optical features (Cox & Bronfman 1995). The clumps, typically a few tenths of a pc across (10–30 arcsec) and with masses of ~ 10 M_⊙, are distributed across a range of velocities (see Table 1). Some of the molecular clumps correspond to those optical features that have bright rims, suggesting the presence of photodissociation regions (PDRs) at the interface with the surrounding ionized gas. PDRs are regions where the far-UV radiation field dominates the heating and chemistry of the gas. They begin at the sharp ionized/neutral interface at the edge of molecular clouds and then extend well into the molecular gas (see Tielens et al. 1993).

To better understand the environment surrounding these clumps we have imaged the Keyhole region at two wavelengths suitable for detecting emission from PDRs. We have used the University of New South Wales Infrared Fabry–Perot (UNSWIRF) to image H₂ 1–0 S(1) (2.122- μ m) emission and the SPIREX/Abu thermal infrared camera at the South Pole to image narrow-band emission at 3.29 μ m. This wavelength includes one of the more prominent ‘unidentified’ infrared (UIR) emission bands and is generally attributed to the C–H stretching mode of free polycyclic aromatic hydrocarbon molecules (PAHs) (Léger & Puget 1984; Allamandola & Tielens 1985; Geballe et al. 1994; Joblin et al. 1995).

H₂ 1–0 S(1) emission in molecular clouds can be attributed to collisional excitation in the presence of shocks or to UV fluorescence in PDRs (see Burton 1992). In dense gas, $n \geq n_{\text{crit}} \sim 10^5 \text{ cm}^{-3}$ where n is the hydrogen nucleus density, UV excitation

[★] E-mail: kbrooks@atnf.csiro.au

[†] Present address: European Southern Observatory, Casilla 19, Santiago, Chile (kbrooks@eso.org).

¹ These data were collected by the Hubble Heritage Team, N. R. Walborn, R. H. Barba and A. Caulet and were released after the submission date of this article (see <http://opposite.stsci.edu/pubinfo/pr/2000/06/pr-photos.html>).

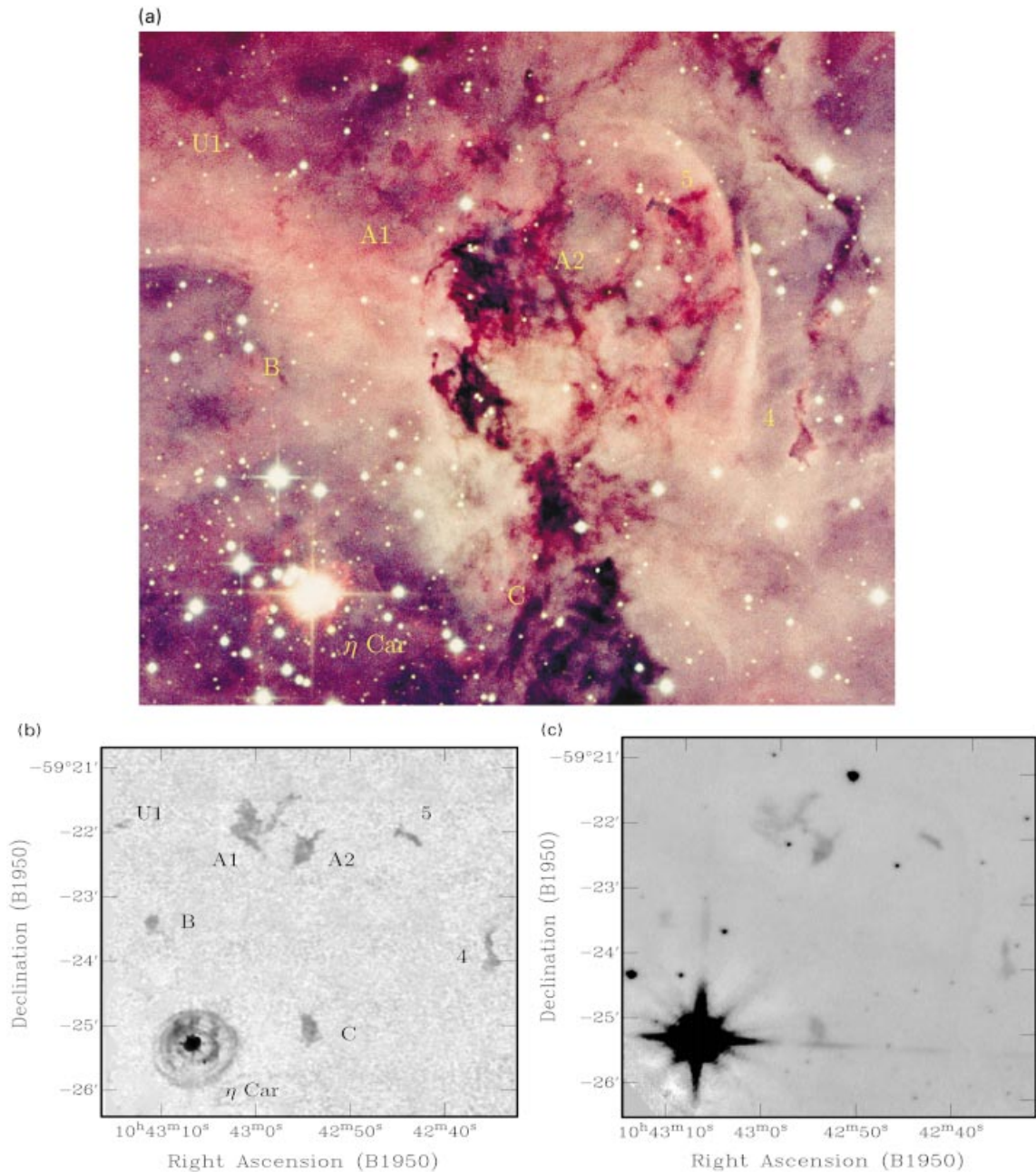


Figure 1. A collection of multiwavelength images of the Keyhole Nebula. Features of interest are labelled in the optical and H₂ 1–0 S(1) images and are described further in Tables 1 and 2. (a) Three-colour optical emission image, courtesy of David Malin. This image was produced by combining three exposures (of 15 min) each taken using blue, green and red filters. The Keyhole is the prominent dark band bisecting the image. (b) H₂ 1–0 S(1) 2.122-μm line emission obtained with UNSWIRF. This image is continuum-subtracted (aside from the circular residuals from η Car). (c) PAH 3.29-μm emission obtained with SPIREX. This image includes continuum sources (the diffraction spikes from η Car are artefacts).

levels are collisionally redistributed, leading to an increase in the population of the $v = 1$ level. This subsequently increases the intensity of the $v = 1-0$ S(1) line (see Allen et al. 1999). Previous observations of PDRs indicate that 3.29-μm PAH emission zones are situated near the very edge of molecular clouds, peaking at the ionization front, while H₂ 1–0 S(1) emission zones extend further into the clouds by about 2 mag of visible extinction (e.g. Sloan et al. 1997; Tielens et al. 1993; Burton et al. 1989). So while H₂ 1–0 S(1) emission cannot be used alone to identify PDRs, if found to correspond to another PDR tracer (such as PAH emission) it can

pinpoint regions of molecular gas that are high in density and exposed to the surrounding far-UV radiation field.

2 OBSERVATIONS

2.1 UNSWIRF observations

UNSWIRF (Ryder et al. 1998) is a near-infrared tunable imaging spectrometer. It was used in conjunction with the Infrared Imager and spectrometer (IRIS) on the Anglo-Australian Telescope

(AAT), and produces a circular field of 1.7 arcmin diameter at 0.77 arcsec pixel⁻¹.

Images of H₂ 1–0 S(1) (2.122- μ m) emission towards the Keyhole region were obtained on 1996 April 24. A series of 30 pointings was made on a 1-arcmin grid at the wavelength of the 2.122- μ m line. An integration time of 60 s was used. An image of the sky was obtained after every five minutes, offset by 5 arcmin from the previous position. This entire sequence was repeated at 3–4 profile widths from the line centre in order to sample the corresponding continuum emission.

Bias subtraction and linearization were performed during readout. All the object images were sky-subtracted and then flat-fielded using normalized dome flat-fields. The continuum images, appropriately scaled, were then subtracted to leave just pure line emission in each. However, the strong emission from η Car prevented a perfect subtraction and so residuals appear in the final image in frames containing η Car. The continuum images were then combined into a mosaic sequence. A coordinate axis was added using a corresponding image obtained with the Digitised Sky Survey (DSS; see http://skyview.gsfc.nasa.gov/cgi-bin/surv_comp.pl?dss) and the program KOORDS (Gooch 1996). The same mosaic sequence and coordinate axis were then applied to the emission-line images. Observations of the spectroscopic standards BS 4013 and HD 105116 were used for the flux calibration and continuum scaling factors. The central wavelength measured varies by up to ~ 10 km s⁻¹ between pixels ($\sim 1/7$ of the FWHM).

Table 1. A list of the ¹²CO(2–1) emission clumps measured by (Cox & Bronfman 1995). The mass measurements may underestimate the true mass of each clump by up to a factor of 3. The type of dark optical feature each clump is associated with is also listed. The velocities are given with respect to the local standard of rest (LSR).

Clump	Velocity (km s ⁻¹)	Mass (M _⊙)	Optical Feature
C	-7.6	6	Faint
B	-8.5	3	Faint
A1 ^a	-17.4	14	Bright rim
A2	-	-	Bright rim
4	-25.0	6	Bright rim
5	-25.1	1	Bright rim
3	-28.3	4	Keyhole (dark)
1	-31.9	17	Keyhole (dark)
2	-32.0	11	Keyhole (dark)

^aAlso known as the ‘Kangaroo Nebula’.

Table 2. Measured H₂ 1–0 S(1) and PAH emission parameters of the clumps shown in Fig 1.

Clump	H ₂ Peak position		H ₂ Peak ^a	PAH Peak ^b	Size	H ₂ Total Intensity	PAH Total Intensity	PAH/H ₂ Ratio
	RA (1950)	Dec. (1950)	($\times 10^{-15}$ erg s ⁻¹ cm ⁻² arcsec ⁻²)	($\times 10^{-14}$ erg s ⁻¹ cm ⁻² arcsec ⁻²)				
A1	10 43 01	-59 22 05	2.1	5.8	60×60	9.9	33	33
A2	10 42 54	-59 22 09	2.7	8.1	20×40	5.5	24	44
B	10 43 11	-59 23 20	1.8	4.7	15×15	1.8	3.6	20
C	10 42 54	-59 25 06	2.8	6.6	15×25	4.4	11	25
4	10 42 35	-59 23 42	2.2	2.8	15×3	3.7	9.1	25
5	10 42 43	-59 22 06	2.5	5.3	25×7	2.3	7.5	33
U1	10 43 14	-59 21 53	1.7	<0.8 ^c	10×10	0.7	<0.1 ^c	<1

^aH₂ image has a 1 σ rms of 0.1×10^{-15} erg s⁻¹ cm⁻² arcsec⁻².

^bPAH image has a 1 σ rms of 3×10^{-15} erg s⁻¹ cm⁻² arcsec⁻².

^c3 σ upper limit.

This can be corrected for by the use of a calibration lamp at closely spaced etalon settings. Normally, line images are then obtained by measuring at several plate spacings (typically 3–5) and fitting the instrumental profile to the line. However, because of the considerable overheads this incurs, this was not attempted for the mapping mode of operation used here. We estimate this introduces an uncertainty of ~ 30 per cent in the line fluxes. The seeing throughout the observations was 1.5 arcsec which, combined with tracking errors and coaddition of frames, produced a positional uncertainty of ± 2.5 arcsec. The final image has a 1 σ rms of 1×10^{-16} erg s⁻¹ cm⁻² pixel⁻¹.

2.2 SPIREX/Abu observations

SPIREX is a 60-cm telescope commissioned in 1994 for operation at the South Pole (Herald et al. 1990). It was equipped in 1998 with the NOAO Abu IR camera (Fowler et al. 1998), which incorporates an engineering grade 1024 \times 1024 ‘Aladdin’ InSb detector array able to image a circular field of view of diameter 10.2 arcmin with a 0.6-arcsec pixel scale.

Observations were carried out on 1998 November 11 (during daylight) using the narrow-band PAH filter. The response curve of this filter covers 3.262–3.336 μ m and is centred on 3.299 μ m, with a half-power width of 0.074 μ m. An integration time of 30 s was used for each frame. The overlapping region from a total of 52 frames was used to obtain a final image of 9 arcmin diameter. The observing sequence consisted of five sky frames followed by 10 object frames. All frames were dark-subtracted and flat-fielded. For the sky subtraction, a scaled median of the six nearest frames, regardless of their actual image type, was subtracted from each object image. The final image contains both PAH emission and continuum emission. A coordinate axis was added using a corresponding image obtained with the Digitised Sky Survey and the program KOORDS.

Observations of the standard star, δ Dor, taken in 1998 November 19, were used for flux calibration (*L*-band magnitude of 3.711 mag). We estimate the PAH fluxes to have an uncertainty of ± 5 per cent. The diffraction limit at 3.3 μ m of the telescope is 1.4 arcsec, comparable to the typical ice-level seeing of the site. However, a combination of tracking errors, tower shake and coaddition of frames limited the pointing accuracy to ± 2.8 arcsec. The final image has a 1 σ rms noise of 2×10^{-15} erg s⁻¹ cm⁻² pixel⁻¹.

The observed wavelength range includes the Pf δ hydrogen recombination line. From the peak Br γ emission flux measured towards the southern edge of clump A1 (6×10^{-15} erg s⁻¹

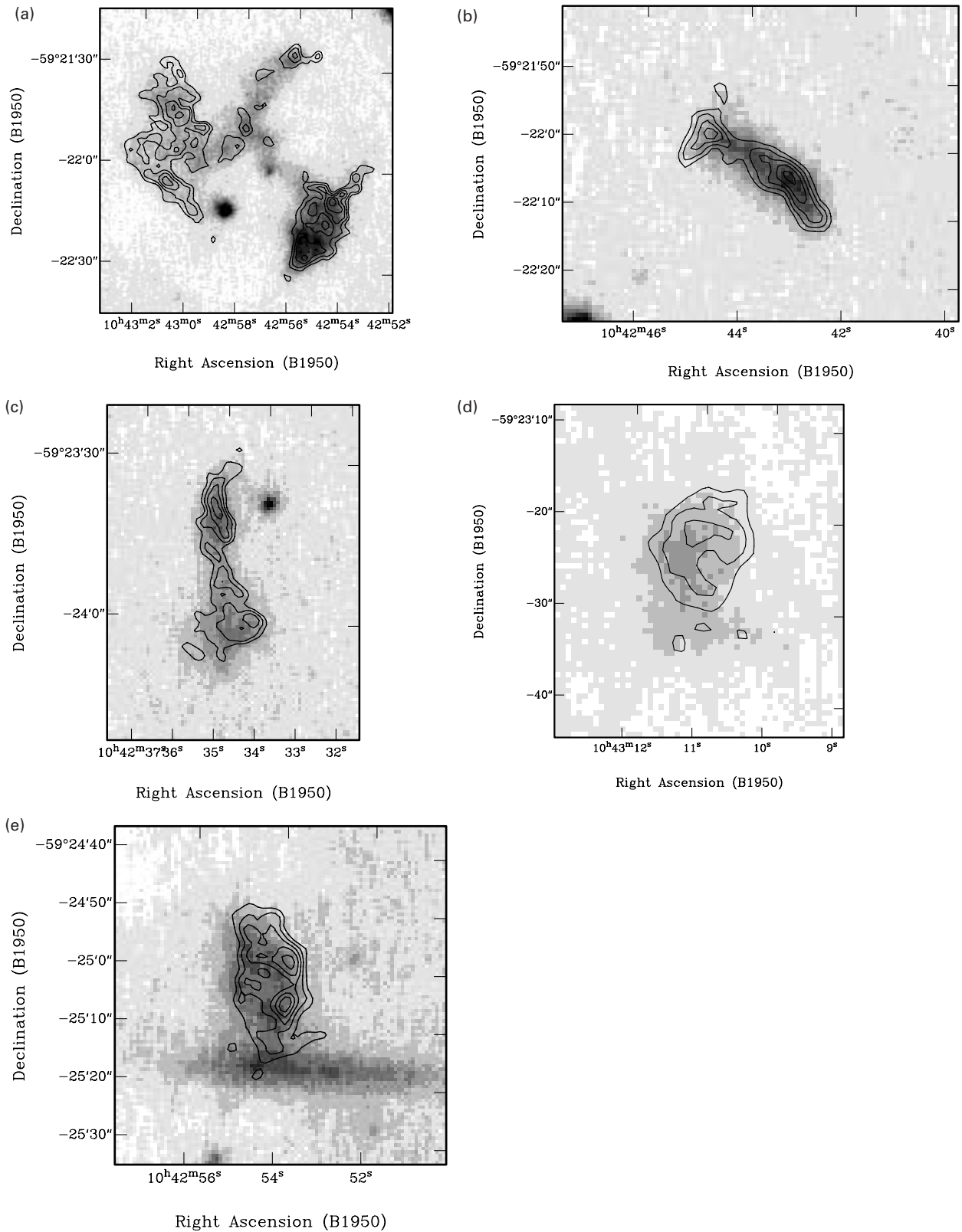


Figure 2. PAH emission in grey-scale format, overlaid with contours of the H_2 1–0 S(1) line emission for Clumps A1 (a), A2 (b), 5 (c), 4 (d), B (e) and C. The contour levels are $5, 8, 12, 15,$ and $19 \times 10^{-16} \text{ erg cm}^{-2} \text{ s}^{-1} \text{ arcsec}^{-2}$. Note the sharp line below Clump C, this is part of the diffraction spike from η Car.

$\text{cm}^{-2} \text{arcsec}^{-2}$) and the calculated relative intensities of the Pf δ and Br γ emission lines (0.26 for the case of $N_e = 10^4 \text{cm}^{-3}$ and $T_e = 10^4 \text{K}$, as listed in table 6 of Hummer & Storey 1987), we estimate that the emission from Pf δ is less than $2 \times 10^{-15} \text{erg s}^{-1} \text{cm}^{-2} \text{arcsec}^{-2}$. This value is the same as the 1σ rms uncertainty of the final $3.29\text{-}\mu\text{m}$ image and therefore we assume that the contribution from the Pf δ line is negligible.

3 RESULTS

Fig. 1(b) shows a map of the H_2 emission towards the Keyhole Nebula. The emission is distributed into seven discrete clumps of less than 1 arcmin in size spread over an area of $4 \times 4 \text{arcmin}^2$. Each emission feature corresponds to a $^{12}\text{CO}(2-1)$ emission clump identified by Cox & Bronfman (1995) and has been labelled accordingly, with the exception of the faint H_2 emission clump located in the north-eastern edge of the image, which we have labelled U1. No CO observations have been made towards this clump. Fig. 1(c) shows an image of the PAH emission over the same region of sky. The emission is also distributed into clumps, all of which (except clump U1) can be matched almost exactly with H_2 emission clumps. This confirms the H_2 emission is caused by UV fluorescence and that the clumps are surrounded by PDRs. Table 2 lists the peak position, peak intensity, total integrated intensity and size of each H_2 emission clump as well as the corresponding PAH peak intensity and total integrated intensity.

Fig. 2 shows the PAH emission as a grey-scale overlaid with contours of H_2 emission for clumps A1,² A2, 4, 5, B and C. The overall distribution of the H_2 and PAH emission is similar for all the clumps, however there are small-scale differences. The emission is not uniform but exhibits many small bright knots and in some cases the H_2 emission knots do not correspond to PAH emission knots. This is to be expected considering that the H_2 and PAH emission zones within a PDR may not completely coincide with one another. The bright H_2 and PAH emission knots are pinpointing high-density regions at different UV optical depths within the molecular clumps.

The ratio of the PAH total intensity to the H_2 1–0 S(1) total intensity is reasonably consistent from clump to clump. Clump A2 has the highest ratio (44), while clump B has the lowest (20).

4 DISCUSSION

4.1 Geometry

Fig. 3 shows the grey-scale H_2 emission with the 4.8-GHz radio continuum emission from Brooks et al. (in preparation) superimposed. The H_2 clumps are distributed around the edges of the continuum emission. The absence of the Keyhole structure in the radio continuum emission indicates that the Keyhole is in the foreground of the nebula and obscuring it.

When comparing the H_2 and PAH emission with the optical emission of Fig. 1(a), it appears that all the emission clumps correspond to dark optical features. Clumps A1, A2, 4 and 5 correspond to prominent patches which have bright rims, while clumps B and C coincide with very faint, filamentary patches. It is worth noting that no H_2 or PAH emission was detected towards the most prominent optical obscuration – the Keyhole itself – or

²We have dubbed clump A1 the ‘Kangaroo Nebula’ owing to its morphological resemblance to an Antipodean marsupial; see Ryder et al. (1998).

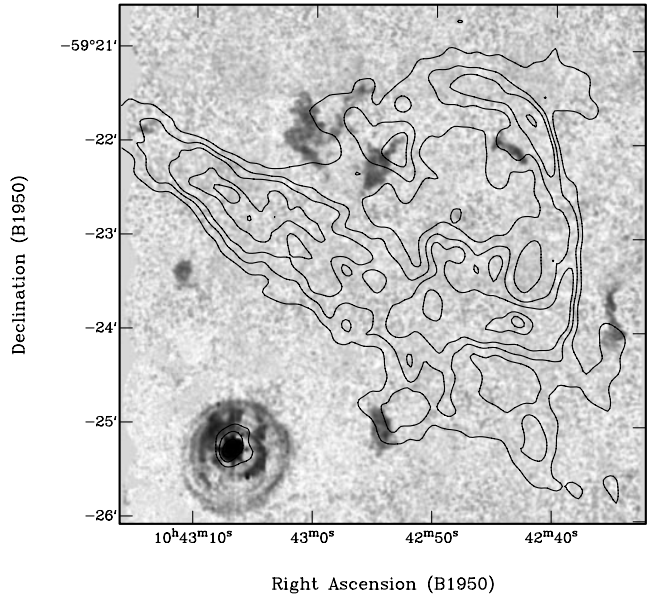


Figure 3. H_2 emission (grey-scale) overlaid with contours of 4.8-GHz continuum emission taken from Brooks et al. (in preparation). The contour levels are 0.02, 0.03, 0.04, 0.05, 0.06, 0.07 Jy beam^{-1} . Note that the contours and emission circles towards η Car are artefacts.

towards the boomerang-shaped filament to the western edge of the image. Neither of these latter two dark features appears to have a bright rim, unlike clumps A1, A2, 4 and 5.

The Keyhole has been traced in $^{12}\text{CO}(2-1)$ emission by Cox & Bronfman (1995) and corresponds to clumps 1, 2, and 3 (see Table 1). These three clumps are the only molecular clumps detected by Cox & Bronfman (1995) which show no H_2 or PAH emission.

As listed in Table 1, the velocities with respect to the local stand of rest (LSR) of the molecular clumps taken from their $^{12}\text{CO}(2-1)$ emission vary from -32 to -8km s^{-1} . When comparing these velocities with the corresponding optical, PAH and H_2 emission features of the clump, there appears to be an interesting trend. First, the clumps with the most negative velocities (clumps 1, 2, and 3) are those that have the most prominent optical obscuration and also the only clumps with no associated PAH and H_2 emission. Secondly, those clumps with intermediate velocities (clumps A1, A2, 4 and 5) correspond to the optical features with bright rims. Thirdly, the clumps which have the least negative velocities (clumps B and C) correspond to the very faint patches. Using these results we present a model for the Keyhole Nebula whereby the velocities of the clumps are associated with positions along our line of sight; clumps 1, 2, and 3 (the Keyhole) are in front of the nebula, clumps A1, A2, 4 and 5 are in it and clumps B and C are located at the far side. This model is represented schematically in Fig. 4.

Radio recombination-line observations of the ionized gas in this region (Car II) reveal a complex velocity structure which has been interpreted as an expanding shell centred close to η Car (Huchtmeier & Day 1975; Deharveng & Maucherat 1975). There are two main velocity components, the relative fluxes of which vary across the region; one having LSR velocities between -6 and -17km s^{-1} and the other having LSR velocities between -23 and -41km s^{-1} . These velocities are consistent with clumps A1, A2, 4 and 5 (i.e. those with bright rims), which have LSR velocities between -17 and -25km s^{-1} , being located in the

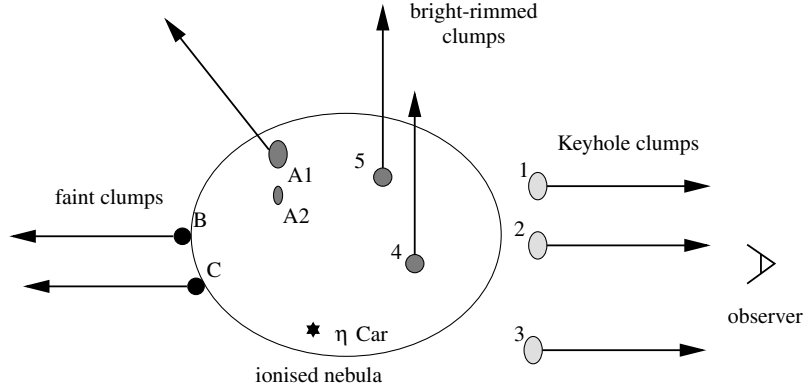


Figure 4. A schematic representation of the three-dimensional geometry of the region, based on the data presented here. The region of ionized gas is bounded by an ellipse and the star denotes the location of η Car. Each clump, with the exception of U1, has been grouped according to its velocity and optical features (see Table 1). The arrows indicate the direction in which the clumps are moving with respect to the ionized gas.

ionized region and the remaining clumps, with LSR velocities near -8 and -30 km s^{-1} , being situated at the far and near side, respectively. The systematic LSR velocity of η Car is taken to be $-18.5 \pm 10 \text{ km s}^{-1}$, similar to the other O-type stars in the region (Davidson et al. 1997), placing it in the middle of the range.

4.2 Dynamics

It is generally thought that the strong stellar winds from the massive stars belonging to Tr 16, in particular η Car, are responsible for the complex dynamics of the ionized and molecular gas in the Keyhole region (e.g. Deharveng & Maucherat 1975; Cox 1995; Cox & Bronfman 1995). Here we extend the analysis of previous studies to include a better estimate of the mechanical luminosity associated with η Car and the energy conversion efficiency factor required to sustain the kinetic energy of a typical clump.

The kinetic energy of a typical clump, K_C , with a mass of $10 M_\odot$ and a velocity of 10 km s^{-1} , is of the order of 10^{46} erg . We can equate this value with the mechanical luminosity, L_W , of the stellar wind of η Car using $K_C \sim L_W \Omega \tau \epsilon$, in order to obtain the required conversion efficiency factor, ϵ . We estimate that the solid angle, Ω , of a typical clump of cross-section 1 arcmin located 3.5 arcmin from η Car is ~ 0.06 . The mechanical luminosity of the wind for η Car, using a mass-loss rate of $5 \times 10^{-4} M_\odot \text{ yr}^{-1}$ (Davidson & Humphreys 1997) and a wind velocity of 700 km s^{-1} (Lamers 1989) is $\sim 8 \times 10^{37} \text{ erg}$. If we take the time period, τ , to be equal to the passage time across the ionized nebula, $\sim 10^5 \text{ yr}$ (2 arcmin at 10 km s^{-1}), then the efficiency factor need only be ~ 0.01 per cent.

In practice τ is likely to be very much less than 10^5 yr , as the clumps will rapidly decelerate as they sweep up material. We estimate its value following Dyson & Williams (1997). They show that the radius of a stellar wind-blown bubble is given by $\sim (L_W/n)\tau^{3/5}$. For a typical clump-mass of $10 M_\odot$, the required density (n) of the swept-up gas is $\sim 1000 \text{ cm}^{-3}$. This yields $\tau \sim 10^3 \text{ yr}$ for the η Car wind, which leads to a required efficiency factor of ~ 1 per cent. This efficiency factor is still much less than the 20 per cent efficiency factor estimated by Dyson & Williams (1997) for this process for a steady wind.

Thus, the kinetic energy of the clumps can readily be explained by the mechanical energy of a wind from η Car. We conclude that the clumps represent swept-up ambient cloud material which is being driven out of the ionized region by such a wind. In this

scenario we would expect the swept-up mass of each clump to be much greater than its wind mass (given by $\dot{M} \Omega \tau / 4\pi$). Substituting the figures above, we obtain $0.003 M_\odot$ for the wind mass, considerably less than the typical swept-up mass of $10 M_\odot$, as expected.

4.3 Excitation

The morphology of the H_2 and PAH emission strongly suggests that UV fluorescence is responsible for the excitation. This conclusion can be quantitatively tested by comparing the observed fluxes with those expected for the physical conditions within the nebula.

We first estimate the ionizing ($h\nu = 13.6 \text{ eV} \rightarrow \infty$) and far-UV ($h\nu = 6 \text{ eV} \rightarrow 13.6 \text{ eV}$) fluxes incident on clump A1 (taken to be 1 arcmin across), from both η Car (3.5 arcmin away) and the O3 star HD 303308 (2.8 arcmin away). HD 303308 is taken to have $T_{\text{eff}} \sim 47500 \text{ K}$ and radius $1 \times 10^{12} \text{ cm}$, following Panagia & Walmsley (1978). Using Kurucz's (1997) model stellar spectra, we find $F_{\text{UV}} = 0.34 \text{ erg s}^{-1} \text{ cm}^{-2}$ and $F_{\text{FUV}} = 0.26 \text{ erg s}^{-1} \text{ cm}^{-2}$. The spectral type of η Car is uncertain. Based on the observations of Cox et al. (1995) at wavelengths longer than $1 \mu\text{m}$, its luminosity has been estimated by Davidson & Humphreys (1997) to be $5 \times 10^6 L_\odot$. At such high luminosities, blackbody and Kurucz models indicate that we can assume the bulk of the flux is distributed over the ionizing and far-UV wavelengths and that $F_{\text{UV}} \sim F_{\text{FUV}}$. Using a stellar radius of $6 \times 10^{12} \text{ cm}$ (Davidson & Humphreys 1997) we find that for η Car $F_{\text{UV}} \sim F_{\text{FUV}} \sim 13 \text{ erg s}^{-1} \text{ cm}^{-2}$, which is considerably greater than the corresponding fluxes from HD 303308.

We thus estimate that the total number of ionizing UV photons incident on clump A1 is $N_{\text{Lycont}} \sim 3 \times 10^{48} \text{ photon s}^{-1}$ and is mostly from η Car. This number is an upper limit, and may be reduced if either internal extinction is present or the distance from the source is greater than its projected value. We have obtained an additional observation of Br γ emission at $2.166 \mu\text{m}$ using UNSWIRF. The total Br γ flux from a region covering 0.7 arcmin^2 , adjacent to the north-west-south-east edge of clump A1, is $3.9 \times 10^{-11} \text{ erg s}^{-1} \text{ cm}^{-2}$. From this, assuming that each Lyman-continuum photon produces 70 Br γ photons, we derive $N_{\text{Lycont}} \sim 2 \times 10^{48} \text{ photon s}^{-1}$, remarkably similar to our estimate based on the stellar luminosities.

We estimate that the total far-UV radiation field on clump A1 is $F_{\text{FUV}} \sim 13 \text{ erg s}^{-1} \text{ cm}^{-2}$, which is equivalent to $\sim 8000 G_0$, where

$G_0 = 1.6 \times 10^{-3} \text{ erg s}^{-1} \text{ cm}^{-2}$ and is the average interstellar radiation field (Habing 1968). Using a far-UV radiation field of $10^4 G_0$ and density of 10^4 cm^{-3} , PDR models (e.g. Burton, Hollenbach & Tielens 1990) predict an H_2 1–0 S(1) line flux of $1.4 \times 10^{-5} \text{ erg s}^{-1} \text{ cm}^{-2} \text{ sr}^{-1}$, which, integrated over a 1-arcmin region, gives a total line flux of $1.2 \times 10^{-12} \text{ erg s}^{-1} \text{ cm}^{-2}$. This is remarkably similar to that measured from clump A1, $9.9 \times 10^{-13} \text{ erg s}^{-1} \text{ cm}^{-2}$ (Table 2). Furthermore, if the density were 10^3 cm^{-3} the prediction would be a factor of 10 smaller, while if the density were 10^5 cm^{-3} it would be a factor of 5 higher. A density of 10^4 cm^{-3} is consistent with CO and CS observations towards clump A1 by Cox & Bronfman (1995), which suggest a value in excess of 10^3 cm^{-3} .

A typical clump with a surface area of 1 arcmin^2 , hydrogen molecule density of 10^4 cm^{-3} and mass of $10 M_\odot$ yields an emitting thickness $A_\nu \sim 1$ (in a direction away from the exciting star) of $\sim 10^{17} \text{ cm}$ (4 arcsec at 2.2 kpc). This order-of-magnitude calculation implies widths similar to those observed for the elongated clumps, 4 and 5, suggesting that they are seen edge-on. These two clumps and the larger clumps, A1 and A2, are thought to be situated inside the H II region (see Fig. 4). Clumps 4 and 5 may be moving edge on, in the plane of the sky, and clumps A1 and A2 may be moving mostly face on, away from us.

The emission measure, $n_e^2 L$, derived from the Br γ line flux is $6 \times 10^5 \text{ cm}^{-6} \text{ pc}$. Taking a typical clump thickness as representative of L gives $L \sim 4 \text{ arcsec}$ (or 0.03 pc based on the above estimate). This yields an electron density $n_e \sim 4 \times 10^3 \text{ cm}^{-3}$ for the ionized gas, which is intermediate in value between the estimates for the initial density and that swept-up in the clumps. The emission measure is also consistent with the value of $2 \times 10^5 \text{ cm}^{-6} \text{ pc}$ obtained from measurements of the 4.8-GHz continuum emission over the same region (Brooks et al., in preparation).

The H_2 and Br γ line emission are thus consistent with UV excitation from η Car. The clumps themselves are swept-up cloud material, likely driven by the mechanical luminosity of a strong wind from η Car. This wind is strong enough to also produce shocked H_2 emission. As there is now no clear evidence for any such emission, this wind cannot still be interacting with the clumps. The clumps must currently be coasting while being externally heated by the radiation field from the nearby stars. Considering the episodic events of η Car's evolution, the current state of the clumps may only represent a quiescent stage in their life and they may be overrun in the future by another fast stellar wind from η Car, resulting in shocked emission. This type of variability, however, would be on time-scales of the order of 1000 yr, considerably longer than the observed 5.54-yr brightness fluctuation cycle of η Car (Damineli, Conti & Lopes 1997).

It is possible to estimate the number of PAH molecules that are emitting from the surfaces of the clumps, using their $3.3\text{-}\mu\text{m}$ flux and the incident far-UV radiation field. Following fig. 13 of Allamandola, Tielens & Barker (1989), the typical energy emitted in the $3.29\text{-}\mu\text{m}$ band by a PAH molecule, excited via far-UV fluorescence to $30\,000 \text{ cm}^{-1}$ of vibrational energy, is $\sim 6 \times 10^{-14} \text{ erg s}^{-1} \text{ molecule}^{-1} \text{ sr}^{-1}$. For an incident far-UV field, $G_0 \sim 10^4$, there are $\sim 10^{12} \text{ photon cm}^{-2} \text{ s}^{-1}$. Taking a typical absorption cross-section for a PAH molecule of $7 \times 10^{-18} \text{ cm}^2$ per C atom (Tielens, private communication), then for a typical 50-atom PAH molecule we expect an excitation rate of $\sim 4 \times 10^{-4} \text{ s}^{-1}$, or about one excitation each hour. This energy is rapidly re-emitted through infrared fluorescence in the various PAH emission bands, including the $3.3\text{-}\mu\text{m}$ band. For the peak $3.29\text{-}\mu\text{m}$ flux of

$3 \times 10^{-3} \text{ erg s}^{-1} \text{ cm}^{-2} \text{ sr}^{-1}$ measured from clump A1, we thus derive an emitting PAH column density of $\sim 10^{14} \text{ cm}^{-2}$ from this region. These estimates show that a significant fraction of the C atoms may reside in PAH molecules. For instance, if the PAH-emitting region were confined to an optical depth $A_\nu < 0.1$ from the front surface of the cloud, it would imply a C abundance in the PAH molecules of $\sim 3 \times 10^{-5}$ relative to hydrogen, or around 30 per cent of the total carbon, assuming typical interstellar carbon abundances.

If the rate of destruction of H_2 molecules by far-UV radiation exceeds their formation rate on dust grains, it is possible that photodissociation equilibrium will not exist in the molecular clumps. For instance, Hollenbach & Natta (1995) derive a characteristic time-scale of $5 \times 10^8 n^{-1} \text{ yr}$ to establish equilibrium. This translates to $\sim 5 \times 10^4 \text{ yr}$ using the densities derived here, which is greater than the assumed age of $\sim 10^3 \text{ yr}$ for the wind. If this were the case, the ionization–dissociation front impinging on the clumps will constantly be exposing fresh molecular material to the radiation field and the fluorescent line intensities will be higher than steady-state model predictions. However the front, moving at perhaps $\sim 1 \text{ km s}^{-1}$, would not have had time to propagate through the clumps. If photodissociation equilibrium does not exist we would expect the ratio of the $\nu = 1\text{-}0/2\text{-}1$ S(1) lines to preferentially show pure fluorescent values (~ 2) where the $\nu = 1\text{-}0$ S(1) line is strongest (see Allen et al. 1999). This could be tested with further observations.

5 CONCLUSIONS

We have imaged the Keyhole region of the Carina Nebula in the H_2 1–0 S(1) line at $2.122 \mu\text{m}$ and in the PAH emission feature at $3.29 \mu\text{m}$, and compared the results with optical, radio continuum and $^{12}\text{CO}(2\text{-}1)$ images of the region. The H_2 and PAH images are remarkably similar, indicating that they are fluorescently excited, and show a series of emission clumps typically 30–60 arcsec in extent distributed around the edges of the radio emission. When compared with the optical and CO images, three categories of clumps are apparent: (i) dark regions of optical obscuration with CO but no H_2 or PAH emission (clumps 1, 2, and 3 which form the Keyhole feature), (ii) faint, optically dark clumps with bright rims and H_2 and PAH emission (clumps A1, A2, 4 and 5) and (iii) faint optically dark clumps with H_2 and PAH emission (clumps B and C).

The clumps are typically of mass $10 M_\odot$ and appear to have been swept up from ambient cloud material by a wind from η Car. They have been driven in all directions away from η Car, and must now be coasting at speeds of $\sim 10 \text{ km s}^{-1}$, as there is no evidence of any shocked emission. The prominent dark clumps of the Keyhole are coming towards us and are outside the H II region. The bright-rimmed clumps A1, A2, 4 and 5 are within the H II region and thus are being heated by the radiation field. Clumps such as A1 are seen face-on whereas clumps 4 and 5 are seen edge-on. Finally the faint dark clumps B and C are on the far side of the H II region and have been driven away from η Car in the opposite direction to ourselves. The clumps comprise the last remnants of the ambient molecular cloud from which η Car formed.

ACKNOWLEDGMENTS

We thank Lori Allen, Stuart Ryder and John Whiteoak for their

help during the observations, and Rodney Marks and members of CARA (the Center for Astrophysical Research in Antarctica), in particular Al Fowler and Al Harper, for obtaining the SPIREX/Abu data. We thank David Malin for providing the colour image of the Keyhole Nebula and Xander Tielens for useful discussions concerning PAH abundances. We are grateful to Stuart Ryder for the UNSWIRF reduction software. We also thank Pierre Cox for helpful comments regarding the manuscript. KJB acknowledges the support of an Australian Postgraduate Award. This work has been supported by a grant from the Australian Research Council.

REFERENCES

- Allamandola L. J., Tielens A. G. G. M., 1985, *ApJ*, 290, L25
 Allamandola L. J., Tielens A. G. G. M., Barker J. R., 1989, *ApJS*, 71, 733
 Allen L. E., Burton M. G., Ryder S. D., Ashley M. C. B., Storey J. W. V., 1999, *MNRAS*, 304, 98
 Burton M. G., 1992, *Aust. J. Phys.*, 45, 463
 Burton M. G., Moorhouse A., Brand P. W. J. L., Roche P. F., Geballe T. R., 1989, in Allamandola L. J., Tielens A. G. G. M., eds, *Proc. IAU Symp.* 135, *Interstellar Dust: contributed papers. NASA CP-3036*, p. 87
 Burton M. G., Hollenbach D. J., Tielens A.G.G.M., 1990, *ApJ*, 365, 620
 Cox P., 1995, *Rev. Mex. Astron. Astrofiz. Ser. Conf.*, 2, 105
 Cox P., Bronfman L., 1995, *A&A*, 299, 583
 Cox P., Mezger P. G., Sievers A., Najarro F., Bronfman L., Kreysa E., Haslam G., 1995, *A&A*, 297, 168
 Damineli A., Conti P. S., Lopes D. F., 1997, *New Astron.*, 2, 107
 Davidson K., Humphreys R. M., 1997, *ARA&A*, 35, 1
 Davidson K., Ebbets D., Johansson S., Morse J. A., Hamann F. W., Humphreys R. M., Weiglet G., Frank A., 1997, *ApJ*, 113, 335
 Deharveng L., Maucherat M., 1975, *A&A*, 41, 27
 Dyson J. E., Williams D. A., 1997, *The physics of the interstellar medium. Inst. Phys. Publ., Bristol*
 Fowler A. M. et al., 1998, *Proc. SPIE*, 3354, 1170
 Geballe T. R., Joblin C., d'Hendecourt L., Jourdain de Muizon M., Tielens A. G. G. M., Léger A., 1994, *ApJ*, 434, L15
 Gooch R., 1996, in Jacoby G. H., Barnes J., eds, *ASP Conf. Ser. Vol. 101, Astronomical Data Analysis Software and Systems V. Astron. Soc. Pac., San Francisco*, p. 80
 Habing H. J., 1968, *Bull. Astr. Inst. Netherlands*, 19, 421
 Hereld M., Rauscher B. J., Harper D. A., Pernic R. J., 1990, *Proc. SPIE*, 1235, 43
 Herschel J. F. W., 1847, *Results of Astronomical Observations Made During the Years 1834–1888 at the Cape of Good Hope. Smith Elder, London*, p. 153
 Hollenbach D., Natta A., 1995, *ApJ*, 455, 133
 Huchtmeier W. K., Day G. A., 1975, *A&A*, 41, 153
 Hummer D. G., Storey P. J., 1987, *MNRAS*, 224, 801
 Joblin C., Tielens A. G. G. M., Allamandola L. J., Léger A., d'Hendecourt L., Geballe T. R., Boissel P., 1995, *Planet. Space Sci.*, 43, 1189
 Kurucz R., 1997
 Lamers H. J. G. L. M., 1989, in Davidson K., Moffat A. F. J., Lamers H.J.G.L.M., eds, *The Physics of Luminous Blue Variables. Kluwer, Dordrecht*, p. 135
 Léger A., Puget J. L., 1984, *A&A*, 137, L5
 Malin D., 1993, *A View of the Universe. Cambridge Univ. Press*, p. 155
 Panagia N., Walmsley C. M., 1978, *A&A*, 70, 411
 Ryder S. D., Sun Y.-S., Ashley M. C. B., Burton M. G., Allen L. E., Storey J. W. V., 1998, *Publications Astronomical Society of Australia*, 15, 228
 Sloan G. C., Bregman J. D., Geballe T. R., Allamandola L. J., Woodward C. E., 1997, *ApJ*, 474, 735
 Tielens A. G. G. M., Meixner M. M., van der Werf P. P., Bregman J., Tauber J. A., Stuzki J., Rank D., 1993, *Sci.*, 262, 86
 Tovmassian H. M., 1995, *Rev. Mex. Astron. Astrofiz. Ser. Conf.*, 2, 83
 Walborn N. R., 1995, *Rev. Mex. Astron. Astrofiz. Ser. Conf.*, 2, 51

This paper has been typeset from a $\text{\TeX}/\text{\LaTeX}$ file prepared by the author.